Front. Chem. Sci. Eng. 2021, 15(4): 944–953
https://doi.org/10.1007/s11705-020-2005-y

RESEARCH ARTICLE

Pyrolysis transformation of ZIF-8 wrapped with polytriazine to nitrogen enriched core-shell polyhedrons carbon for supercapacitor

Nuoya Wang[1], Xinhua Huang (✉)[1], Lei Zhang[1], Jinsong Hu[2], Yimin Chao[3], Ruikun Zhao (✉)[4]

1 School of Materials Science and Engineering, Anhui University of Science and Technology, Huainan 232001, China
2 School of Chemical Engineering, Anhui University of Science and Technology, Huainan 232001, China
3 School of Chemistry, University of East Anglia, Norwich, NR4 7TJ, UK
4 College of Arts and Sciences, Khalifa University of Science and Technology, Abu Dhabi, UAE

Abstract This work presents a simple effective strategy to synthesize *N*-doped and shell-controlled carbon nanocages through a package baking approach. A green approach to synthesize core-shell ZIF-8@PTZ nanoparticles involves zinc contained ZIF-8 core wrapped by a N-enriched polytriazine (PTZ). Synthesized core-shell ZIF-8@PTZ nanoparticles are calcinated to further sublime zinc through PTZ shell and washed by HCl, leaving a porous carbon structure. At the meantime, hollow cavities were introduced into N-doped carbon polyhedrons via the sacrifice of ZIF-8 template (noted as ZIF-8@C/N-x). The electrochemical performance of the ZIF-8@C/N-x as supercapacitor electrode has demonstrated high energy density and specific capacitance, as well as a long-term cycleability showing 92% capacitance retention after 10000 cycles. There is a systematic correlation between micro-/meso-porosity of ZIF-8@C/N-x and their electrochemical performances.

Keywords core-shell, EDLC electrode, microporos nano polygons, nitrogen doped carbon

1 Introduction

Supercapacitors, are the most potential energy storage devices for lithium battery substituent alternatives, owing to their high-power densities and fast charge-discharge performances [1−4]. It has been proved in practice that carbon nanomaterials are the best choice as the supercapacitor electrode [5−7]. Carbon-based materials inherit many natural features, such as excellent stability; high conductivity; economy-friendly and ease to synthesis, which have been widely used for many energy supply implements [8−10]. Generally speaking, the electrochemical performances of carbon materials are determined by the synergies of their specific surface areas, pore distributions, and the heteroatoms doped [11,12]. Various carbon-based nanomaterials for the applications in supercapacitors have been developed in the past decades [13−15].

Metal organic frameworks (MOFs) are often used as the precursors that sacrifice later for preparing porous carbon framework as a result of their high surface areas and adjustable pore structures [16−18]. Furthermore, N-enriched MOFs yields N-doped porous carbon can increase their carbon materials' hydrophilicities and conductivities beneficial for their electrochemistry performance [19−21]. However, the direct high-temperature carbonization of MOFs could collapse the regular structure and decrease the surface areas although the N atoms are to be released easily during the pyrolysis. It is therefore necessary to preserve the structures with N atom containing molecules [22−24]. For example, Zhang et al. using Prussian-blue as the core and functionalized with N (or P)-doped carbon demonstrated high performance in electrocatalysis [25,26]. Zhu et al. reported ZnO@MOF@PANI core-shell nanoarrays on carbon cloth for high-performance supercapacitor electrodes [27]. Apparently, it has been evidenced that using second carbon source on modified MOFs can enable the tuning of the structure and enhance the electrochemical performance.

Zinc involving MOFs, specifically the zeolitic imidazolate framework (ZIF-8), could be simply prepared with an accessible experiment in water at ambient temperature. Afterwards, zinc can be sublimed from the mold and

Received May 16, 2020; accepted August 6, 2020

E-mails: xhhuang@aust.edu.cn (Huang X);
ruikun.zhao@ku.ac.ae (Zhao R)

results in N-containing carbon material to form micropores. In literature, ZIF-8-poly(cyclotriphosphazene-hexahydroxytriphenylene) [28], ZIF-8@CTAB [29], ZIF-8@PVP [30], ZIF-8/urea [31] and ZIF-8@GO [32] are employed to produce the nitrogen-doped hierarchically porous carbon at a high temperature. However, the complex preparation processes of carbon MOFs limit the mass production with serious environmental pollutions. The preparation of electrodes from carbon nanomaterials for supercapacitors should be easy and environment-friendly, and most importantly the performance should meet the needs [33,34].

This study presents an approach of using N-enriched polytriazine (PTZ) as the second carbon source to wrap ZIF-8, which through the package baking to synthesize porous and high N-doped carbon nanocages. During carbonization in the high-temperature, the zinc sublimation produces pores in the obtained carbon matrix, while the PTZ shell is transformed to N coexisted carbon nanopolyhedrons with cavities, which are resulted from the sacrificial ZIF-8 template. A series of samples with different PTZ shell thicknesses have been synthesized by the formation of the core-shell ZIF-8@C/N-x nanopolyhedrons and pyrolyzation at high temperature. The electrochemical performances of supercapacitors using ZIF-8@C/N-x electrodes have shown an explicit dependency on degree of N-doping and microporosity. As a result, we have fabricated an electric double-layer capacitors electrode and demonstrated high specific capacitance, power & energy densities, as well as long-term cycling stability.

2 Experimental

2.1 Materials preparations

All chemicals were acquired from Alfa Aesar and directly applied in the experiments. The detailed synthesis processes are as follows: 1) Synthesis of ZIF-8 in aqueous solution. The synthesis of ZIF-8 refers to the synthesis method in literature [35]. Firstly, 0.744 g of $Zn(NO_3)_2 \cdot 6H_2O$ was dissolved in 10 mL of deionized water, and 12.3 g of dimethylimidazole was dissolved in 90 mL of deionized water. Then, the two solutions were mixed by stirring for 24 h at ambient temperature. The ZIF-8 solution was prepared with a concentration of 4 $mg \cdot mL^{-1}$. 2) ZIF-8@PTZ. Initially, 10 mL, 20 mL, and 30 mL ZIF-8 solutions were prepared in three 1 L glass cups respectively, and distilled water was added to reach the volumes all to 600 mL exactly. Then 2,6-diaminopyridine (300 mg) and formaldehyde (450 μL) were added under vigorous stirring for 18 h at room temperature. The crude samples were collected after centrifuge and washed with deionized water and methanol, purified in a Soxhlet extractor for 48 h, followed by drying at 80 °C to obtain powder samples. 3) ZIF-8@C/N-x. Under N_2 atmosphere, the dried samples were placed in tube furnace at 600 °C for 5 h, then at 915 °C for 1 h to obtain the zinc contained sample. The sample was soaked in 3 $mol \cdot L^{-1}$ HCl overnight to remove zinc, then rinsed repeatedly with deionized water before dried at 80 °C to obtained the ZIF-8@C/N-x: x is the sample serial number, representing adding 10, 20 and 30 mL of ZIF-8 solutions, respectively. The samples were named based on the amount of ZIF-8 during the synthesis process, as ZIF-8@C/N-1, ZIF-8@C/N-2, ZIF-8@C/N-3.

2.2 Electrochemical measurement

A two-electrode system test was performed using an electrochemical workstation (CHI 760E, CH Instrument, Shanghai) in 6 $mol \cdot L^{-1}$ KOH electrolyte. The sample, acetylene black, and polyvinylidene fluoride were mixed in N-methyl pyrrolidone at a mass ratio of 8:1:1 to form a slurry and coated on nickel foam. Nickel foam was continued for 1 min under a pressure of 10 MPa, then dried at 80 °C to make an electrode. The mass of the active material on one electrode was about 1 to 2 mg, and the mass difference between the two electrodes does not exceed 0.2 mg. The calculation on the single electrode mass ratio capacitance was based on the galvanostatic charge/discharge (GCD) test. The calculation formula is given as below:

$$C = 4\ (I \times \Delta t)/(m \times \Delta U). \tag{1}$$

The gravimetric energy density of the device E ($W \cdot h \cdot kg^{-1}$) and P ($W \cdot kg^{-1}$) was calculated with the equation below:

$$E = 1/2\ (C \times \Delta U^2), \tag{2}$$

$$P = 3600E/\Delta t, \tag{3}$$

where I is the constant current in a constant current charge-discharge curve, m is the total mass of the electrode, Δt is the discharge time, and ΔU is the discharge voltage.

2.3 Materials characterizations

Scanning electron microscope (SEM) and transmission electron microscope (TEM) analysis were carried out with a JEOL JEM-2100F instrument and JEOL, 1400 PLUS instrument respectively. X-ray diffraction (XRD) measurements were conducted by X-ray diffractometer (Smartlab SE, Rigaku Ltd., Japan) with Cu radiation (λ = 0.154 nm). Raman spectroscopy was measured at room temperature with Renishaw Invia RM200 (UK), under the condition of λ_{exc} = 514 nm, laser excitation was performed at exposure time and excitation power of 10 s and 20 mW, respectively. Nitrogen (77 K) sorption isotherms were measured from

relative pressure P/P_0 of 6.9×10^{-8} to 0.992 using a Micromeritics ASAP 2020 analyzer. The conventional Brunauer-Emmett-Teller (BET) method and density functional theory method showed the specific surface area and pore size distributions.

3 Results and discussion

Scheme 1 shows the schematic diagram of the synthetic route of ZIF-8@C/N-x. At room temperature, formaldehyde and 2,6-diaminopyridine were polymerized in a dispersed ZIF-8 aqueous solution for 18 h to form a PTZ. The ZIF-8 nanoparticles functioned as the core before being wrapped in a PTZ shell, then the system was baked at a temperature of 915 °C to have the zinc sublimed at 907 °C under N_2 atmosphere [28]. ZIF-8 is in high nitrogen mass percentage, which can be conserved in the skeleton framework of the porous carbon pro-carbonization [36]. As well known, N-doped carbon as energy storage devices can enhance the conductivity, wettability with aqueous electrolyte and pseudo-capacitance [19]. However, N in the ZIF-8 unavoidably lost during the carbonization processes at high temperature. According to the recent literatures [37], PTZ has been employed as the secondary N sources to prevent the N loss and protect the framework of ZIF-8, in addition to improving the electrochemical performance, which can be easily synthesized in water at room temperature the same as ZIF-8. During the process of annealing, Zn^{2+} from the core of the ZIF-8 polyhedrons converted to metallic zinc by reduction reaction before subliming to the surface of PTZ shell, leaving micro-/meso-porosity into the PTZ shell. At the end of annealing, the PTZ shell is modified to carbon retaining hollow polygons with cavity generated from core ZIF-8 polyhedrons. The carbonized sample was soaked in 3 $mol \cdot L^{-1}$ HCl overnight to remove remaining Zn in the sample, and finally polygonal porous carbon ZIF-8@C/N-x were obtained.

The FE-SEM and TEM images in Fig. 1 clearly shows that the ZIF-8@C/N-x has a hollow polyhedrons cavity with a side length of 100 nm (Figs. 1(a–c)), and the thickness of the shell varies from 29 to 22 nm (Figs. 1(d–f) inset) with the volume of ZIF-8 added in the precursors. The monomer of PTZ spontaneously polymerized outside of ZIF-8 with its polyhedrons structure formed. This is because the ZIF-8 can be the active core as the polycondensation of PTZ, it also explains the shell of the ZIF-8@C/N-x changed to thin while increasing the ZIF-8 content under the same polymerization concentration. The corresponding EDS maps of C, N, and O in Fig. 1(g) shows the C/N shell is perfectly wrapped on the ZIF-8 solid core of the ultimate ZIF-8@C/N-2.

The Raman spectrum in Fig. 2(a) shows the I_D/I_G band intensity ratios of ZIF-8@C/N-x. The G (1580 cm^{-1}) peak arises from the vibrational mode of sp^2 bonded graphite carbon [36–38], while the D (1345 cm^{-1}) band in the ZIF-8@C/N-x carbon becomes the prominent feature of the Raman spectrum [39], the high I_D/I_G (> 1) band intensity ratio of the ZIF-8@C/N-x is attributed for nitrogen doping [40] from the carbon precursors, which is beneficial for the charge transfer in the adsorption process [41].

XRD spectrum further characterizes the structure of ZIF-8@C/N-x. As shown in Fig. 2(b), two broad diffraction peaks appeared at ~23° (2θ) and ~42° (2θ). The two reflections associated with the (002) and (100) planes of graphite indicates the dominant features in amorphous carbon [42]. There are no characteristic peaks of zinc in XRD spectrum, and combined with XPS analysis (Fig. 2(c)), it was found that most of the Zn in the sample has been removed, which does not have much impact on subsequent characterization.

The full XPS spectrum further evidenced the C, N, and O in ZIF-8@C/N-x samples. Table 1 shows the percentage of N atoms based on the XPS data (wide scan in Fig. 2(c)). When the ZIF-8 increased during the preparation process, the atomic percentage of N also increased, which suggests that the imidazole component in the ZIF-8 template provided a part of N for the sample [28], meanwhile, the external C/N shell provided by PTZ does offset the nitrogen loss of the ZIF-8 during the carbonization. Pyridinic nitrogen (N-6), pyrrolic nitrogen (N-5), graphitic nitrogen (N-Q), and chemisorbed nitrogen oxides (N-X) are shown in the high-resolution N1s spectrum, corre-

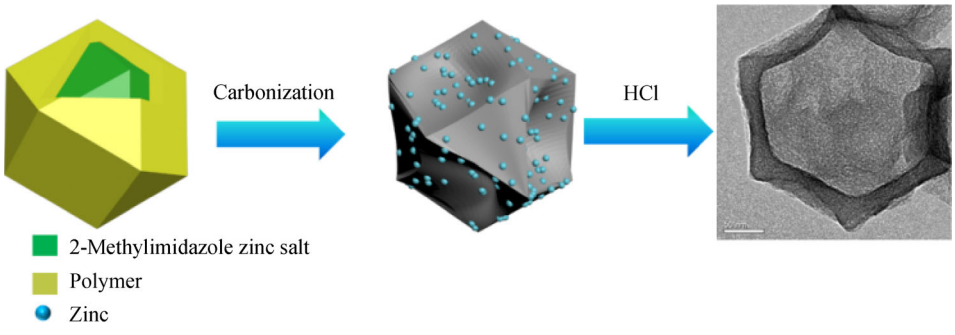

Scheme 1 Schematic illustration for the formation of ZIF-8@C/N-X.

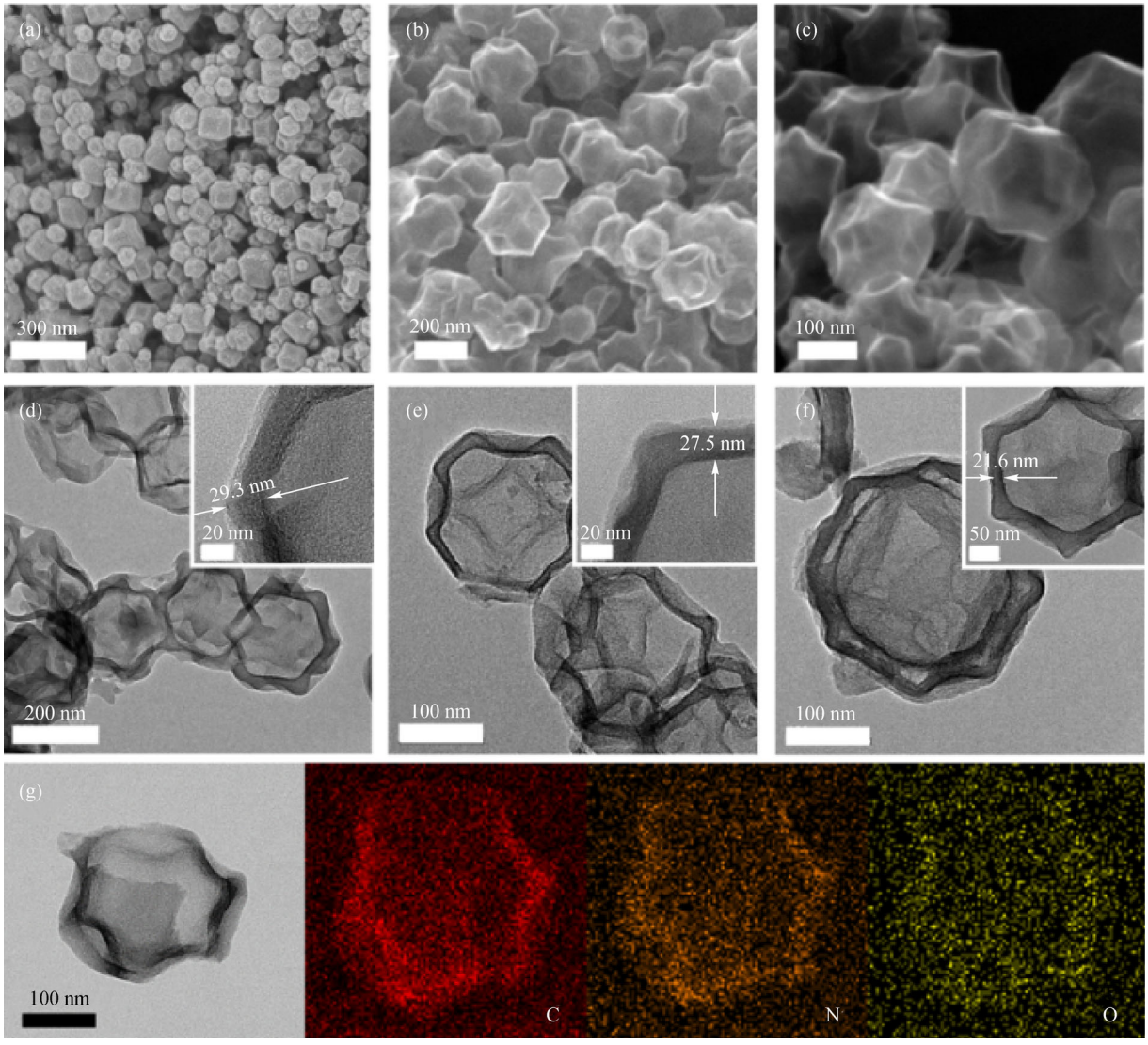

Fig. 1 SEM images of (a) ZIF-8@C/N-1, (b) ZIF-8@C/N-2 and (c) ZIF-8@C/N-3; TEM images of (d) ZIF-8@C/N-1, (e) ZIF-8@C/N-2 and (f) ZIF-8@C/N-3 and the inset is the shell of C/N from corresponding PTZ; (g) The TEM images of ZIF-8@C/N-2 with element EDS mapping for C, N, O.

Table 1 Nitrogen composition of ZIF-8@C/N-x

Sample	N/wt-%	N-6/wt-%	N-5/wt-%	N-Q/wt-%	N-X/wt-%
ZIF-8@C/N-1	19.57	27.34	6.61	42.39	23.66
ZIF-8@C/N-2	21.76	27.72	15.98	40.68	15.62
ZIF-8@C/N-3	22.24	18.42	22.44	40.08	19.06

sponding to 397.6, 398.5, 399.9 and 402.4 eV in the spectrum (Fig. 2(d)), respectively. Frankly speaking, the N-5 and N-6 are with characteristics of electron donors with high charge mobility, which could behave as active electrochemical active sites to capacitance increasing. On the other hand, the N-Q also improves the carbon material's conductivity by performing as electron donors and/or protons attractors, which could stimulate the redox reaction and enhance the rate performances [42−45]. The total content of N-5, N-6, N-Q in the N atoms of the sample is above 80%, which improves the specific capacitance of the sample. At the meantime, the presence of O atoms in the sample also provides a pseudo-capacitance to the sample and enhances the surface electrode's invasiveness [46−48].

The pore characteristics of all samples were analyzed by

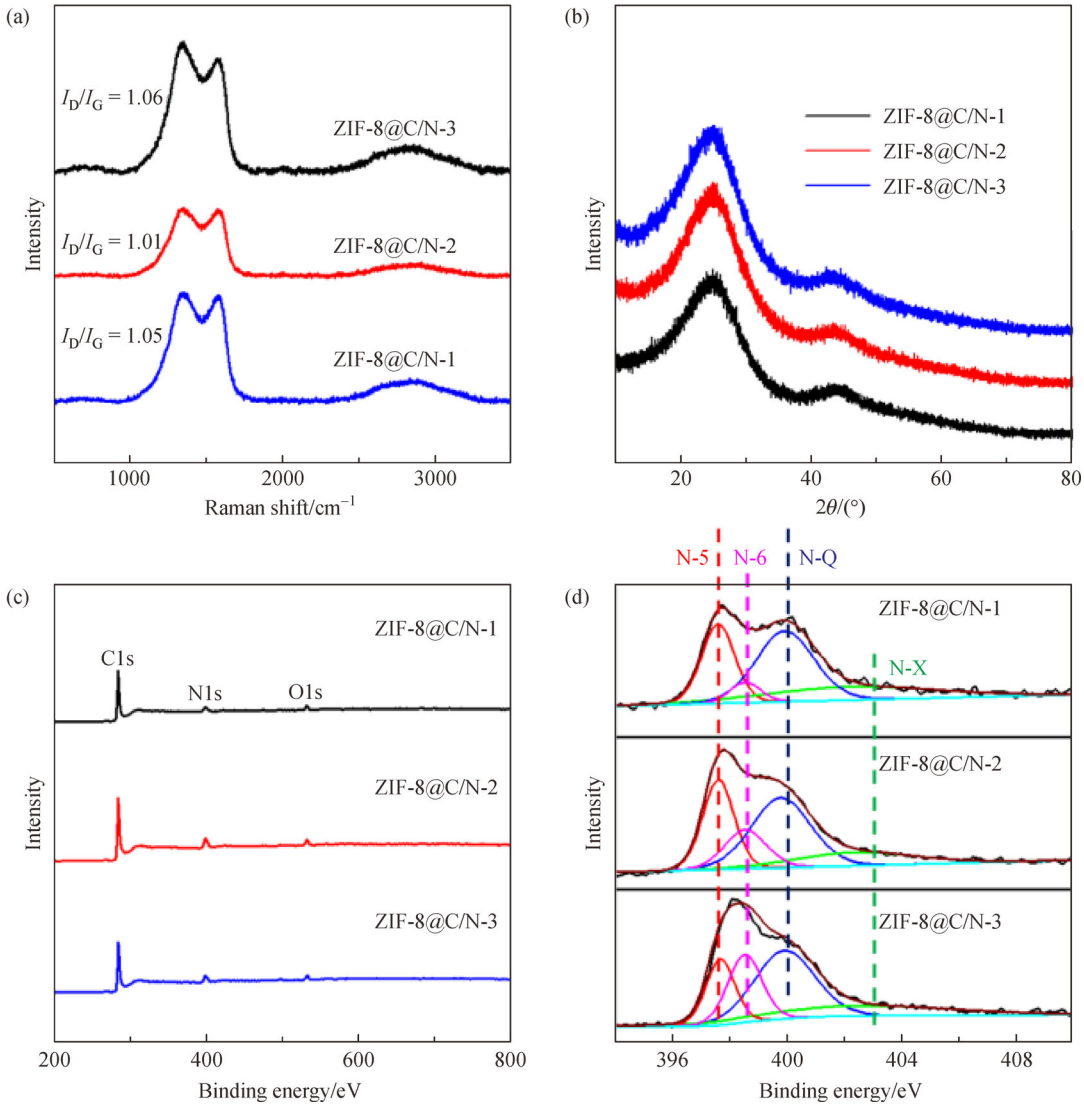

Fig. 2 (a) Raman spectra and (b) XRD patterns of the ZIF-8@C/N-x samples, (c) XPS and (d) high-resolution XPS spectra of N1s the ZIF-8@C/N-x samples.

a N_2 adsorption-desorption (Fig. 3(a)). ZIF-8@C/N-1, 2 display type I sorption isotherms generated from microporous solids having relatively small external surfaces (e.g., molecular sieve zeolites, activated carbons, COFs/MOFs and certain porous oxides), while ZIF-8@C/N-3 displays a type IV sorption isotherm with type H4 hysteresis loop resulting from the mesopores [49,50]. The structural feature as mentioned above is further supported by the pore size distribution curves (Fig. 3(b)) and the averaged pore size was found to be 8.1−12.6 nm among the three ZIF-8@C/N-x samples (Table 2). The narrower pore size distribution of ZIF-8@C/N-x, the larger percentage of microporous surface area which is over 58% (e.g., 80% micropores of ZIF-8@C/N-3), ascribed to the Zinc sublimation and the PTZ after carbonization produced [50].

Figure 4(a) presents the galvanostatic charge/discharge (GCD) curves with a current density of 0.5 $A \cdot g^{-1}$ of ZIF-8@C/N-x, as well as the GCD curves at various current densities are shown in Figs. S1(a,c,e) (cf. Electronic Supplementary Material, ESM). The curve of ZIF-8@C/N-x slightly deviates from the linear shape which shows the presence of pseudo-capacitance [51]. Besides, ZIF-8@C/N-2 shows a much longer charge/discharge time than other samples, suggesting a higher specific capacitance value. This result suggests that more surfaces in ZIF-8@C/N-2 become accessible for electrolyte ions [52]. Figure 4(b) shows the cyclic voltammetry (CV) curves of ZIF-8@C/N electrodes at a scan rate of 200 $mV \cdot s^{-1}$ in 6 $mol \cdot L^{-1}$ KOH. All curves display a quasi-rectangular shape, indicating the synergistic contribution is from electric double-layer and faradaic capacitances. The CV curves were deformed

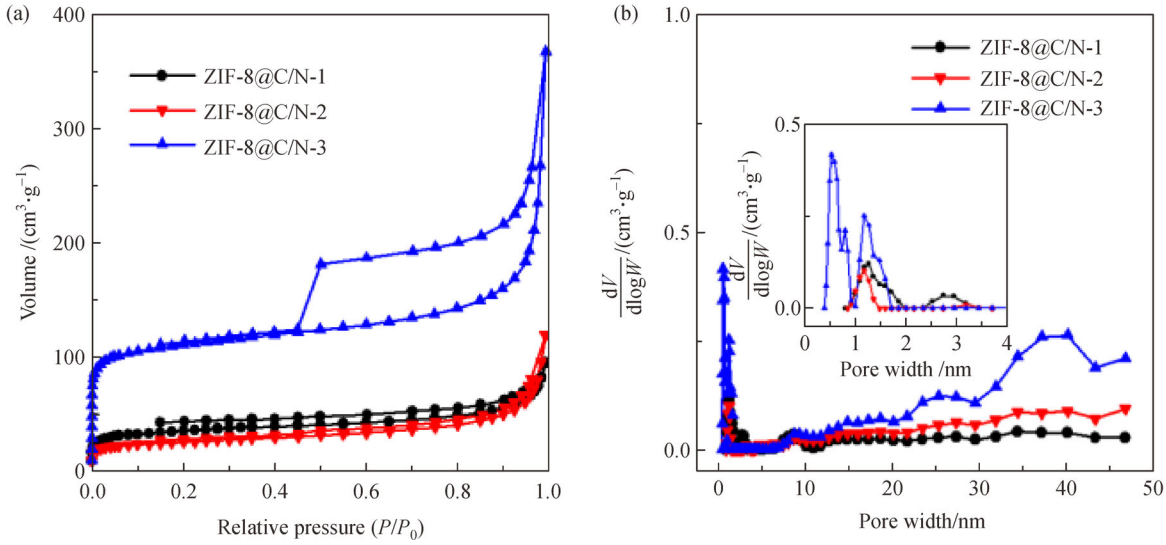

Fig. 3 (a) N_2 adsorption/desorption isotherms and (b) pore size distribution of ZIF-8@C/N-x.

Table 2 Porosity data of ZIF-8@C/N-x

Sample	S_{BET} a)/($m^2 \cdot g^{-1}$)	Pore volume/($cm^3 \cdot g^{-1}$)	S_{micro} b)/($m^2 \cdot g^{-1}$)	S_{meso} c) /($m^2 \cdot g^{-1}$)	$\%_{micro}$ d)	Pore size/nm
ZIF-8@C/N-1	133	0.148	101.9	31.1	76	12.6
ZIF-8@C/N-2	93.9	0.185	54.6	39.3	58	14.8
ZIF-8@C/N-3	423.3	0.57	340	83.3	80	8.1

a) S_{BET}: specific surface area; b) S_{micro}: micropore surface area; c) S_{meso}: mesopore surface area; d) $\%_{micro}$: the S_{micro} percent in the S_{BET}.

which is mainly due to a surface redox reaction happened in the N-5 and N-6 carbon matrix [53]. Additionally, the CV curve area of ZIF-8@C/N-2 is larger than other samples, which is consistent with the GCD results, indicating the highest capacitive property due to the highest N-5 and N-6 content from ZIF-8@C/N-2 (Table 1) even though it quite poor porosities. The CV curves at various scan rates are shown in Figs. S1(b,d,f), and the rectangular-like shape is maintained even swept at 500 $mV \cdot s^{-1}$, reflecting its excellent rate performances. The specific capacitance of the single electrode calculated from the GCD curves at different current densities (Table S1, cf. ESM) is shown in Fig. 4(c), and the specific capacitance decreases with increasing current density. The Nyquist plots of ZIF-8@C/N-x are presented in Fig. 4(d). The EIS analysis is a common method to study the conductivity and the charge transfer behaviors for electrode materials [54]. All the samples pointed low series resistance (R_s) values, suggesting that all ZIF-8@C/N-x samples had low intrinsic resistances and charge transfer resistances. As can be seen from the inset in Fig. 4(d), ZIF-8@C/N-2 has lower intrinsic resistances and charge transfer resistances compared to other samples. The inset of Fig. 4(d) shows the enlarged view of high frequency region and equivalent circuit diagram. The high frequency intercept along the x-axis represents the equivalent R_s, a combination of the ionic resistance of the electrolyte, the intrinsic resistance of the electrode material and interface resistance of the active material/current collector. The R_s of 1.11, 0.87 and 1.08 Ω for ZIF-8@C/N-1, 2 and 3, respectively, are observed from the intercept at the real axis. The semicircle in the high frequency region stands for the interfacial charge-transfer resistance (R_{ct}) between the electrode and electrolyte. The R_{ct} value for ZIF-8@C/N-2 was 0.31 Ω, which was lower than that of pure ZIF-8@C/N-1 (0.62 Ω) and ZIF-8@C/N-3 (0.71 Ω). In the lower frequency region, all Nyquist plots displayed a nearly vertically straight line, demonstrating the low ion diffusion/transport resistance or the Warburg element (W). Figure 4(e) shows the Ragone plots of ZIF-8@C/N-2 based on the specific capacitances in the two-electrode system. Apparently, there is a minor decrease occurred in energy density of the electrode material with increasing the power density for both carbons. The energy density decreased from 13.43 $W \cdot h \cdot kg^{-1}$ to 8.05 $W \cdot h \cdot kg^{-1}$ as power density increased from 250 $W \cdot kg^{-1}$ (0.5 $A \cdot g^{-1}$) to 5576.73 $W \cdot kg^{-1}$ (10 $A \cdot g^{-1}$), implying that the decrease of the energy density is not really significant. This is similar to most carbon materials [37,55−58]. In Table S2 (cf. ESM), the electrochemical performance of ZIF-8@C/N-2 is compared with the N-C materials reported in the past two years. It can be seen intuitively that ZIF-8@C/N-2

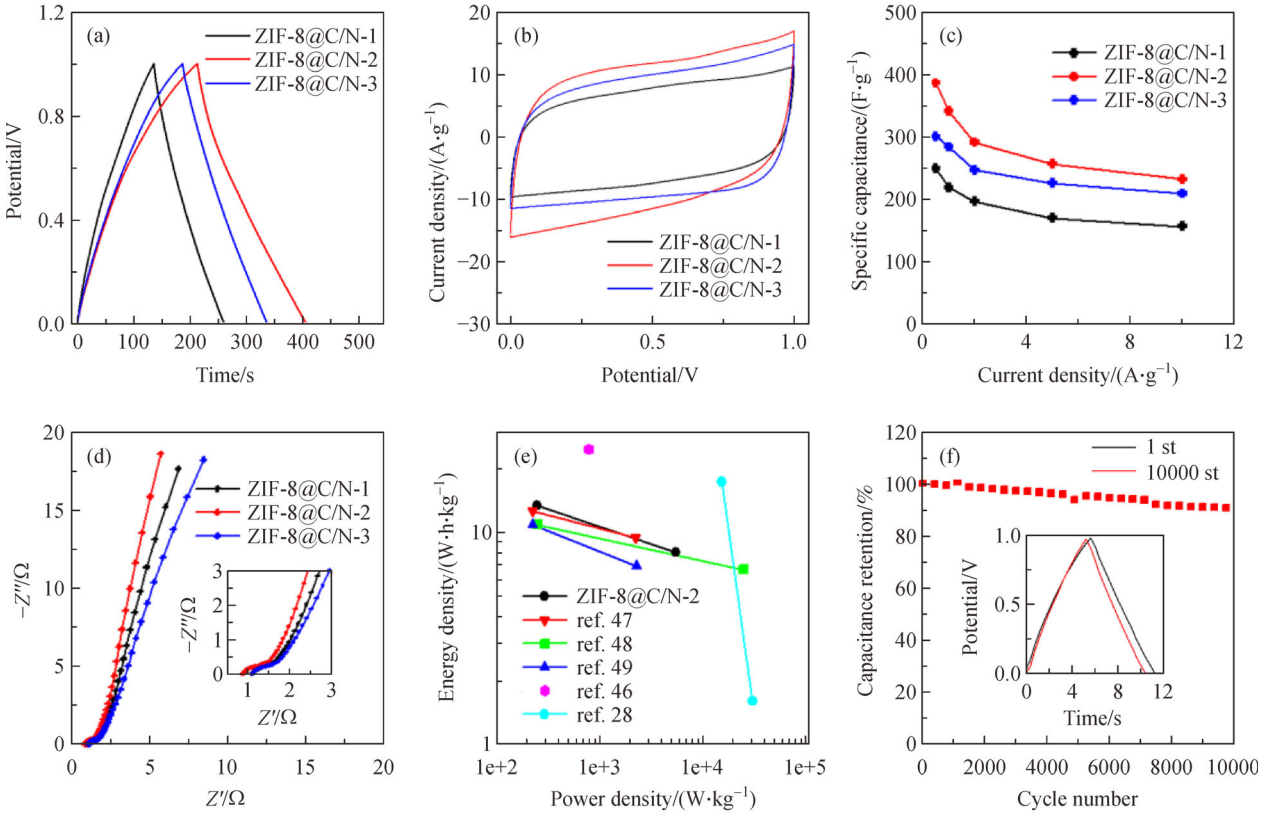

Fig. 4 (a) GCD curves and (b) CV curves of the as-prepared samples at a current density of 0.5 $A \cdot g^{-1}$ and at a scan rate of 200 $mV \cdot s^{-1}$; (c) specific capacitances of the as-prepared samples at different current densities and (d) EIS of the as-prepared samples at the open circuit potential in the frequency range from 0.1 to 10^5 Hz; (e) Ragone plot (energy density vs. power density) of ZIF-8@C/N-2, another report's data are added for comparison, and (f) cyclic stability (current density of 10 $A \cdot g^{-1}$)

material has certain advantages compared with other materials, its energy density is higher than most N-C materials and has a higher specific capacitance. Ragone plots of all the four types of ZIF-8@C/N-x based electrodes are shown in Fig. S2 (cf. ESM). In addition, the cycle life of the ZIF-8@C/N-2 electrodes is tested. Typically (Fig. 4(f)), after charge and discharge for 10000 cycles at a current density of 10 $A \cdot g^{-1}$, the ZIF-8@C/N-2 electrode retains 92% of the initial capacitance and the charge-discharge curves maintain a triangular shape.

4 Conclusions

In summary, the solid ZIF-8 nanoparticles have been wrapped in a nitrogen-containing PTZ to create a core-shell structure with different shell thicknesses. As a result, the core-shell ZIF-8@C/N-x nanoparticles were carbonized to ZIF-8@PTZ in high temperatures, shell thickness can be rational adjusted based on the ratio of wrapped PTZ. The porosity of derived PTZ could be precisely controlled by varying thicknesses of the shell due to its affection on zinc sublimation in the ZIF-8 core. The N% percentage in C/N shell was significantly affected by the preservation of the N releasing from ZIF-8 and its self-carbonization. The application of ZIF-8@C/N-x in super capacitor electrodes shows that the micro-and meso-pores of ZIF-8@C/N-x are playing vital role in the electrochemical performance. The highest specific capacitance of ZIF-8@C/N-2 (386.8 $F \cdot g^{-1}$ at current density of 0.5 $A \cdot g^{-1}$) has been accomplished at an average diameter of 14.8 nm and 58% of micropore percentage. The ZIF-8@C/N-x in symmetric super-capacitors has shown significant high capacitance, high power and energy densities, as well as long-term capacitance cycling durability (92% retention at 10000 cycles). This green approach for synthesizing core-shell N-doped carbon nanomaterials provides a great potential for future materials in electrochemical applications such as electro-catalysts, Li-ion batteries, super-capacitors.

Acknowledgements This work was supported by the Key Project of Natural Science Research in Anhui Colleges and Universities (KJ2017A070), Anhui Province Natural Science Foundation Project (1908085ME157), and Anhui Province Selective Foundation of Innovation Project for Study Abroad (2019LCX020).

Electronic Supplementary Material Supplementary material is available in the online version of this article at https://doi.org/10.1007/s11705-020-2005-y and is accessible for authorized users.

References

1. Muzaffar A, Ahamed M B, Deshmukh K, Thirumalai J. A review on recent advances in hybrid supercapacitors: design, fabrication and applications. Renewable & Sustainable Energy Reviews, 2019, 101: 123–145
2. Sharma K, Arora A, Tripathi S K. Review of supercapacitors: materials and devices. Journal of Energy Storage, 2019, 21: 801–825
3. Lu X F, Wang A L, Xu H, He X J, Tong Y X, Li G R. High-performance supercapacitors based on MnO_2 tube-in-tube arrays. Journal of Materials Chemistry. A, Materials for Energy and Sustainability, 2015, 3(32): 16560–16566
4. Xu H, Zhang C, Zhou W, Li G R. $Co(OH)_2$/RGO/NiO sandwich-structured nanotube arrays with special surface and synergistic effects as high-performance positive electrodes for asymmetric supercapacitors. Nanoscale, 2015, 7(40): 16932–16942
5. Faraji S, Ani F N. The development supercapacitor from activated carbon by electroless plating—a review. Renewable & Sustainable Energy Reviews, 2015, 42: 823–834
6. Li X, Wei B. Supercapacitor based on nanostructure carbon. Nano Energy, 2013, 2: 159–173
7. Zhang L L, Zhao X S. Carbon-based materials as supercapacitor electrodes. Chemical Society Reviews, 2009, 38(9): 2520–2531
8. Lu X F, Li G R, Tong Y X. A review of negative electrode materials for electrochemical supercapacitors. Science China. Technological Sciences, 2015, 58(11): 1799–1808
9. Wang T, Li H G, Shi S J, Liu T, Yang G, Chao Y M, Yin F. 2D film of carbon nanofibers elastically astricted MnO microparticles: a flexible binder-free anode for highly reversible lithium ion storage. Small, 2017, 13(20): 1604182
10. Chen L, Yan B, Xu J, Wang C G, Chao Y M, Jiang X F, Yang G. Bicontinuous structure of $Li_3V_2(PO_4)_3$ clustered via carbon nanofiber as high-performance cathode material of Li-ion batteries. ACS Applied Materials & Interfaces, 2015, 7(25): 13934–13943
11. Wang L, Chen L, Yan B, Wang C G, Zhu F, Jiang X F, Chao Y M, Yang G. *In situ* preparation of SnO_2@polyaniline nanocomposites and their synergetic structure for high-performance supercapacitors. Journal of Materials Chemistry. A, Materials for Energy and Sustainability, 2014, 2(22): 8334–8341
12. Ji H M, Ma C, Ding J J, Yang J, Yang G, Chao Y M, Yang Y. Complementary stabilization by core/sheath carbon nanofibers/spongy carbon on submicron tin oxide particles as anode for lithium-ion batteries. Journal of Power Sources, 2019, 413: 42–49
13. Wang Q, Yan J, Fan Z. Carbon materials for high volumetric performance supercapacitors: design, progress, challenges and opportunities. Energy & Environmental Science, 2016, 9(3): 729–762
14. Chen X, Paul R, Dai L. Carbon-based supercapacitors for efficient energy storage. National Science Review, 2017, 4(3): 453–489
15. Huang J S, Sumpter B G, Meunier V. Theoretical model for nanoporous carbon supercapacitors. Angewandte Chemie International Edition, 2008, 47(3): 520–524
16. Yang S J, Kim T, Im J H, Kim Y S, Lee K, Jung H, Park C R. MOF-derived hierarchically porous carbon with exceptional porosity and hydrogen storage capacity. Chemistry of Materials, 2012, 24(3): 464–470
17. Chaikittisilp W, Ariga K, Yamauchi Y. A new family of carbon materials: synthesis of MOF-derived nanoporous carbons and their promising applications. Journal of Materials Chemistry. A, Materials for Energy and Sustainability, 2013, 1(1): 14–19
18. Ren Q, Wang H, Lu F X, Gong Y X, Li G R. Recent progress on MOF-derived heteroatom-doped carbon-based electrocatalysts for oxygen reduction reaction. Advancement of Science, 2017, 5(3): 1700515
19. Li W H, Hu S H, Luo X Y, Li Z L, Sun X Z, Li M S, Liu F F, Yu Y. Confined amorphous red phosphorus in MOF-derived N-doped microporous carbon as a superior anode for sodium-ion battery. Advanced Materials, 2017, 29(16): 1605820
20. Chai L L, Zhang L J, Wang X, Xu L Q, Han C, Li T T, Hu Y, Qian J J, Huang S M. Bottom-up synthesis of MOF-derived hollow N-doped carbon materials for enhanced ORR performance. Carbon, 2019, 146: 248–256
21. Ren Q, Wang H, Lu X F, Tong Y X, Li G R. Recent progress on MOF-derived heteroatom-doped carbon-based electrocatalysts for oxygen reduction reaction. Advancement of Science, 2018, 5(3): 1700515
22. Liu Y, Miao W, Fang X, Tang Y L, Wu D L, Mao S. MOF-derived metal-free N-doped porous carbon mediated peroxydisulfate activation via radical and non-radical pathways: role of graphitic N and C–O. Chemical Engineering Journal, 2020, 380: 122584
23. Yang H X, Zhao D L, Meng W J, Zhao M, Duan Y J, Han X Y, Tian X M. Nickel nanoparticles incorporated into N-doped porous carbon derived from N-containing nickel-MOF for high-performance supercapacitors. Journal of Alloys and Compounds, 2019, 782: 905–914
24. Zhao L Y, Yu J, Xing C T, Ullah Z, Yu C C, Zhu S P, Chen M L, Li W W, Li Q, Liu L W. Nanopore confined anthraquinone in MOF-derived N-doped microporous carbon as stable organic cathode for lithium-ion battery. Energy Storage Materials, 2019, 22: 433–440
25. Zhang L, Hu J S, Huang X H, Song J, Lu S Y. Particle-in-box nanostructured materials created via spatially confined pyrolysis as high performance bifunctional catalysts for electrochemical overall water splitting. Nano Energy, 2018, 48: 489–499
26. Lv C N, Zhang L, Huang X H, Zhu Y X, Zhang X, Hu J S, Lu S Y. Double functionalization of N-doped carbon carved hollow nanocubes with mixed metal phosphides as efficient bifunctional catalysts for electrochemical overall water splitting. Nano Energy, 2019, 65: 103995
27. Zhu C M, He Y, Liu Y J, Kazantseva N, Saha P, Cheng Q L. ZnO@MOF@PANI core-shell nanoarrays on carbon cloth for high-performance supercapacitor electrodes. Journal of Energy Chemistry, 2019, 35: 124–131
28. Kale V S, Hwang M, Chang H, Kang J, Chae S I, Jeon Y, Yang J, Kim J, Ko Y J, Piao Y, Hyeon T. Microporosity-controlled synthesis of heteroatom codoped carbon nanocages by wrap-bake-sublime

approach for flexible all-solid-state-supercapacitors. Advanced Functional Materials, 2018, 28(37): 1803786
29. Jiang M, Cao X P, Zhu D D, Duan Y X, Zhang J M. Hierarchically porous N-doped carbon derived from ZIF-8 nanocomposites for electrochemical applications. Electrochimica Acta, 2016, 196: 699–707
30. Lai Q X, Zhao Y X, Liang Y Y, He J P, Chen J H. *In situ* confinement pyrolysis transformation of ZIF-8 to nitrogen-enriched meso-microporous carbon frameworks for oxygen reduction. Advanced Functional Materials, 2016, 26(45): 8334–8344
31. Ma X C, Li L Q, Zeng Z, Chen R F, Wang C H, Zhou K, Su C Q, Li H L. Synthesis of nitrogen-rich nanoporous carbon materials with C_3N-type from ZIF-8 for methanol adsorption. Chemical Engineering Journal, 2019, 363: 49–56
32. Ding B, Fan Z J, Lin Q Y, Wang J, Chang Z, Li T, Henzie J, Kim J, Dou H, Zhang X G, et al. Confined pyrolysis of ZIF-8 polyhedrons wrapped with graphene oxide nanosheets to prepare 3D porous carbon heterostructures. Small Methods, 2019, 3(11): 1900277
33. Chen Y Z, Wang C M, Wu Z Y, Xiong Y J, Xu Q, Yu S H, Jiang H L. From bimetallic metal-organic framework to porous carbon: high surface area and multicomponent active dopants for excellent electrocatalysis. Advanced Materials, 2015, 27(34): 5010–5016
34. Feng J X, Ye S H, Wang A L, Lu X F, Tong Y X, Li G R. Flexible cellulose paper-based asymmetrical thin film supercapacitors with high-performance for electrochemical energy storage. Advanced Functional Materials, 2014, 24(45): 7093–7101
35. Tanaka S, Kida K, Okita M, Ito Y, Miyake Y. Size-controlled synthesis of zeolitic imidazolate framework-8 (ZIF-8) crystals in an aqueous system at room temperature. Chemistry Letters, 2012, 41 (10): 1337–1339
36. Ferrari A C, Robertson J. Interpretation of Raman spectra of disordered and amorphous carbon. Physical Review. B, 2000, 61 (20): 14095–14107
37. Huang X H, Wang N Y, Li F, Zhu X X, Liao K, Chan V, Zhang L. Molecular engineering of supercapacitor electrodes with monodispersed N-doped carbon nanoporous spheres. New Journal of Chemistry, 2019, 43(40): 15892–15898
38. Zhu J, Kong L R, Shen X P, Chen Q R, Ji Z Y, Wang J H, Xu K Q, Zhu G X. Three-dimensional N-doped graphene/polyaniline composite foam for high performance supercapacitors. Applied Surface Science, 2018, 428: 348–355
39. Zhang S, Sui L, Kang H Q, Dong H Z, Dong L F, Yu L Y. High performance of N-doped graphene with bubble-like textures for supercapacitors. Small, 2018, 14(5): 1702570
40. Dai S G, Liu Z, Zhao B T, Zeng J H, Hu H, Zhang Q B, Chen D C, Qu C, Dang D, Liu M L. A high-performance supercapacitor electrode based on N-doped porous graphene. Journal of Power Sources, 2018, 387: 43–48
41. Liu Y, Pan L K, Chen T Q, Xu X T, Lu T, Sun Z, Chua D H C. Porous carbon spheres via microwave-assisted synthesis for capacitive deionization. Electrochimica Acta, 2015, 151: 489–496
42. Zou K X, Deng Y F, Chen J P, Qian Y Q, Yang Y W, Li Y W, Chen G H. Hierarchically porous nitrogen-doped carbon derived from the activation of agriculture waste by potassium hydroxide and urea for high-performance supercapacitors. Journal of Power Sources, 2018, 378: 579–588
43. Liu T Y, Zhang F, Song Y, Li Y. Revitalizing carbon supercapacitor electrodes with hierarchical porous structures. Journal of Materials Chemistry. A, Materials for Energy and Sustainability, 2017, 5(34): 17705–17733
44. Ouyang T, Cheng K, Gao Y, Kong S, Ye K, Wang G, Cao D. Molten salt synthesis of nitrogen doped porous carbon: a new preparation methodology for high-volumetric capacitance electrode materials. Journal of Materials Chemistry. A, Materials for Energy and Sustainability, 2016, 4(25): 9832–9843
45. Wang D W, Li F, Yin L C, Lu X, Chen Z G, Gentle I R, Lu G Q, Cheng H M. Nitrogen-doped carbon monolith for alkaline supercapacitors and understanding nitrogen-induced redox transitions. Chemistry (Weinheim an der Bergstrasse, Germany), 2012, 18(17): 5345–5351
46. Song Z Y, Zhu D Z, Xue D F, Yan J J, Chai X L, Xiong W, Wang Z W, Lv Y K, Cao T C, Liu M X, et al. Nitrogen-enriched hollow porous carbon nanospheres with tailored morphology and microstructure for all-solid-state symmetric supercapacitors. ACS Applied Energy Materials, 2018, 1(8): 4293–4303
47. Zhao G Y, Chen C, Yu D F, Sun L, Yang C H, Zhang H, Sun Y, Besenbacher F, Yu M. One-step production of O–N–S co-doped three-dimensional hierarchical porous carbons for high-performance supercapacitors. Nano Energy, 2018, 47: 547–555
48. Xue D F, Zhu D Z, Liu M X, Duan H, Li L C, Chai X L, Wang Z W, Lv Y K, Xiong W, Gan L H. Schiff-base/resin copolymer under hypersaline condition to high-level N-doped porous carbon nanosheets for supercapacitors. ACS Applied Nano Materials, 2018, 1(9): 4998–5007
49. Kim W, Joo J B, Kim N, Oh S, Kim P, Yi J. Preparation of nitrogen-doped mesoporous carbon nanopipes for the electrochemical double layer capacitor. Carbon, 2009, 47(5): 1407–1411
50. Tang J, Liu J, Li C L, Li Y Q, Tade M O, Dai S, Yamauchi Y. Synthesis of nitrogen-doped mesoporous carbon spheres with extra-large pores through assembly of diblock copolymer micelles. Angewandte Chemie International Edition, 2015, 54(2): 588–593
51. Gao F, Shao G H, Qu J Y, Lv S Y, Li Y Q, Wu M B. Tailoring of porous and nitrogen-rich carbons derived from hydrochar for high-performance supercapacitor electrodes. Electrochimica Acta, 2015, 155: 201–208
52. Zhang X S, Yan P T, Zhang R J, Liu K, Liu Y Y, Liu T, Wang X Y. A novel approach of binary doping sulfur and nitrogen into graphene layers for enhancing electrochemical performances of supercapacitors. Journal of Materials Chemistry. A, Materials for Energy and Sustainability, 2016, 4(48): 19053–19059
53. Hou S J, Wang M, Xu X T, Li Y D, Li Y J, Lu T, Pan L K. Nitrogen-doped carbon spheres: a new high-energy-density and long-life pseudo-capacitive electrode material for electrochemical flow capacitor. Journal of Colloid and Interface Science, 2017, 491: 161–166
54. Hulicova D, Yamashita J, Soneda Y, Hatori H, Kodama M. Supercapacitors prepared from melamine-based carbon. Chemistry of Materials, 2005, 17(5): 1241–1247
55. Xin L J, Li R M, Lu Z T, Liu Q, Chen R R, Li J Q, Liu J Y, Wang J. Hierarchical metal-organic framework derived nitrogen-doped porous carbon by controllable synthesis for high performance supercapacitors. Journal of Electroanalytical Chemistry (Lausanne,

Switzerland), 2018, 813: 200–207
56. Li X Q, Hao C L, Tang B C, Wang Y, Liu M, Wang Y W, Zhu Y H, Lu C G, Tang Z Y. Supercapacitor electrode materials with hierarchically structured pores from carbonization of MWCNTs and ZIF-8 composites. Nanoscale, 2017, 9(6): 2178–2187
57. Chen L F, Lu Y, Yu L, Lou X W D. Designed formation of hollow particle-based nitrogen-doped carbon nanofibers for high-performance supercapacitors. Energy & Environmental Science, 2017, 10 (8): 1777–1783
58. Salunkhe R R, Kamachi Y, Torad N L, Hwang S M, Sun Z, Dou S X, Kim J H, Yamauchi Y. Fabrication of symmetric supercapacitors based on MOF-derived nanoporous carbons. Journal of Materials Chemistry. A, Materials for Energy and Sustainability, 2014, 2(46): 19848–19854